ORIGINAL RESEARCH

# Design, Fabrication and Analysis of Silicon Hollow Microneedles for Transdermal Drug Delivery System for Treatment of Hemodynamic Dysfunctions

**M. W. Ashraf · S. Tayyaba · A. Nisar ·
N. Afzulpurkar · D. W. Bodhale · T. Lomas ·
A. Poyai · A. Tuantranont**

**Abstract** In this paper, we present design, fabrication and coupled multifield analysis of hollow out-of-plane silicon microneedles with piezoelectrically actuated microfluidic device for transdermal drug delivery (TDD) system for treatment of cardiovascular or hemodynamic disorders such as hypertension. The mask layout design and fabrication process of silicon microneedles and reservoir involving deep reactive ion etching (DRIE) is first presented. This is followed by actual fabrication of silicon hollow microneedles by a series of combined isotropic and anisotropic etching processes using inductively coupled plasma (ICP) etching technology. Then coupled multifield analysis of a MEMS based piezoelectrically actuated device with integrated silicon microneedles is presented. The coupledfield analysis of hollow silicon microneedle array integrated with piezoelectric micropump has involved structural and fluid field couplings in a sequential structural-fluid analysis on a three-dimensional model of the microfluidic device. The effect of voltage and frequency on silicon membrane deflection and flow rate through the microneedle is investigated in the coupled field analysis using multiple code coupling method. The results of the present study provide valuable benchmark and prediction data to fabricate optimized designs of the silicon hollow microneedle based microfluidic devices for transdermal drug delivery applications.

**Keywords** Computational fluid dynamic (CFD) analysis · Deep reactive ion etching (DRIE) · Drug delivery · Hollow silicon microneedle · Multifield analysis · Transdermal drug delivery (TDD)

M. W. Ashraf (✉) · S. Tayyaba · A. Nisar · N. Afzulpurkar ·
D. W. Bodhale
School of Engineering and Technology,
Asian Institute of Technology (AIT), Bangkok, Thailand
e-mail: Muhammad.Waseem.Ashraf@ait.ac.th

T. Lomas · A. Tuantranont
Nanoelectronics and MEMS Lab,
National Electronics and Computer Technology Center
(NECTEC), Bangkok, Thailand

A. Poyai
Thai Microelectronics Center (TMEC), Bangkok, Thailand

## Introduction

Transdermal drug delivery (TDD) systems deal with the movement of pharmaceutical compound through the skin to reach the systemic circulation for subsequent distribution in the human body. TDD systems consist of non-invasive and minimally invasive technologies for delivering drugs and vaccines across the skin (Barry 2001; Prausnitz 2004; Schuetz et al. 2005). TDD devices can be divided into active and passive devices based on the technologies used for skin permeation. In passive devices, the methods used for skin permeation are chemical enhancers, emulsions, and lipid assemblies as well as biological methods such as peptides (Prausnitz 2004; Schuetz et al. 2005; Schreier and Bouwstra 1994; Karande et al. 2004). A recent trend towards increasing use of active methods for skin permeation has been reported by Brown et al. (2006). The most common active methods of skin permeation are jet injectors, iontophoresis, electroporation, ultrasound, microneedles, powder injection, ablation, and tape stripping (Arora et al. 2008). One of the major drawbacks of TDD systems has been their inability to deliver the drugs through the skin within the desired therapeutic range. To overcome this limitation, many studies have been conducted on new drug delivery methods using emerging micro and nanotechnologies. The

major focus of MEMS for drug delivery has been towards the development of microneedles for minimally invasive TDD applications. Using MEMS technology, microneedles with various sizes, shapes, and materials have been fabricated. In vitro and in vivo studies have shown successful applications of solid microneedles in terms of skin permeability for a broad range of molecules, DNA vaccines, and nanoparticles.

A MEMS based microneedle is a needle with diameter and length in micrometers. A microneedle is different from standard hypodermic needles used in medical applications as generally the length of the MEMS based microneedles is less than 1 mm. Thus microneedles are significantly smaller in length than ordinary needles. Based on the fabrication process, the microneedles are classified as in-plane and out-of-plane microneedles. In in-plane microneedles, the microneedle shaft is parallel to the substrate surface. A major advantage of in-plane microneedles is that length of the microneedle can be easily and accurately controlled during the fabrication process. The limitation of in-plane microneedles is that it is difficult to fabricate microneedle arrays with two dimensional geometry. In out-of-plane microneedles, the length of the microneedles protrudes out of the substrate surface and it is easier to fabricate out-of-plane microneedles in arrays. However, fabrication of out-of-plane microneedles with length and high aspect ratio structure is a challenging task in microfabrication. Another significant distinction that can be made in microneedles is whether microneedles are solid or hollow. Hollow microneedles have an internal bore or lumen which allows flow of fluid or drug through the microneedles. Microneedles also vary according to the structure, tip shape and overall shape. The details of microneedle categories are shown in Table 1.

Campbell et al. (1991) reported one of the earliest out-of-plane microneedle array consisted of 100 microneedles with a length of 1.5 mm. The microneedles were fabricated to stimulate the visual cortex of the brain for sight treatment. Similarly in-plane microneedles have been used for activity recording and cellular chemostimuli of brain tissue (BeMent et al. 1986; Chen et al. 1997). Solid, out-of-plane,

microneedles have been used to penetrate the stratum corneum layer in human skin (outermost layer of the epidermis is the stratum corneum, a 10–20 μm layer) for Electroencephalogram (EEG) measurements for anesthesia monitoring (Griss et al. 2001, 2002). Oka et al. (2002) reported fabrication of microneedles for blood collection. Mukherjee et al. (2004) demonstrated sampling of body fluids by capillary action achieved with 350 μm long hollow out-of-plane microneedles. Zahn et al. (2004) fabricated microneedles for microdialysis applications. Although there are other application fields for microneedles, however a majority of microneedles reported so far in the literature are concerned with drug delivery in different applications (Bodhale et al. 2009). Design and development of MEMS based microneedles is strongly dependent on the fabrication process. Majority of existing microfabrication technologies have been derived from processes developed to fabricate integrated circuits. Photolithography is the most common and powerful of these fabrication technologies. A schematic illustration of microfabrication of tapered projections using photolithography is shown in Fig. 1.

A number of other processes have been developed such as polymer replication, polymer lamination, soft lithography and fabrication by using high aspect ratio photosensitive resins such as SU-8 photoresist. In these processes silicon and polymer can be used as substrate materials for microfabrication. However, application of silicon as the substrate material is still dominant because of some excellent mechanical and electrical properties and the possibility to directly integrate circuit on the transducer's substrate. With the help of anisotropic etching process, deep holes or free standing structures can be fabricated in silicon. These high aspect ratio structures are of considerable interest in developing microdevices for various applications. With the help of anisotropic etching process, high aspect ratio structures can be easily fabricated and this process is generally referred to as deep reactive ion etching (DRIE) process. Silicon is anisotropically etched by DRIE process in a commercially available etching machine called inductively coupled plasma (ICP) etcher. ICP etcher

**Table 1** Categories of microneedles

| Material | Overall shape | Tip shape | Structure | Application |
|---|---|---|---|---|
| Polymers | Cylindrical | Volcano | Solid/hollow | Drug delivery |
| Silicon | Pyramid | Snake fang | In-plane/Out-of-plane | Blood extraction |
| Silicon dioxide | Candle | Micro-hypodermis | | Fluid sampling |
| Silicon nitride | Spike | | | Cancer therapy |
| Glass | Spear | | | Micro-dialysis |
| Semiconductor (extrinsic) | Square | | | Ink-jet printing |
| Metal | | | | Electrodes for sensing |
| Alloys | | | | |
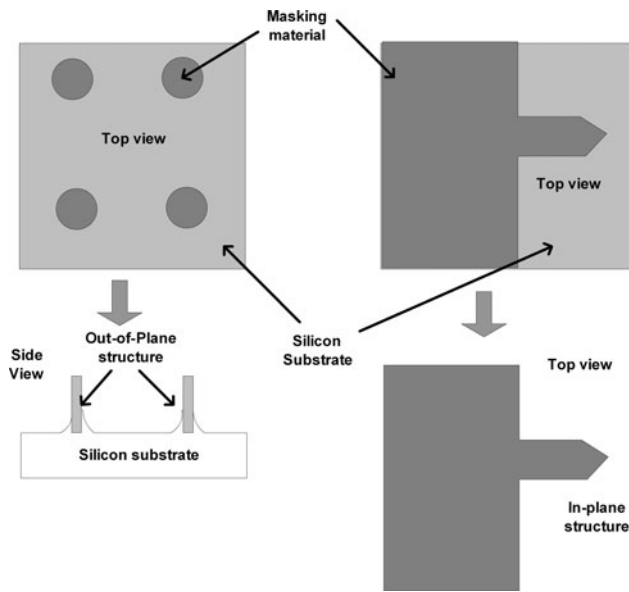
**Fig. 1** Schematic illustration of microfabrication of tapered projections

fabrication process involves a plasma source and a combination of sequential etching and polymer deposition. ICP etcher uses $SF_6$ gas for etching cycle and $C_4F_8$ gas for passivation cycle. In ICP etching process, plasma and gas pressure/flow parameters need to be controlled to achieve desired etch characteristics and profile. The most significant work on microneedles for TDD applications began in 1998 when Henry et al. (1998) reported fabrication of 150 μm long solid silicon microneedle using DRIE process. Park et al. (2003, 2005) fabricated biodegradable polymer microneedles by vacuum casting of polyglycolic acid in a silicon mold. Hollow microneedles with reservoirs have been developed for TDD to eliminate problem of fluctuation in daily dosage to reduce side effects. Kim et al. (2004) fabricated out-of-plane hollow metallic microneedles with SU-8 mold and backside exposure by metal deposition technology. Moon and Lee (2005) developed inclined lithography, galvanoformung and abformung (LIGA) process to fabricate microneedle array using polymethylmethacrylate (PMMA). Micromachining methods in metal and polymer have their own limitations; therefore the above mentioned methods are complicated to fabricate microneedles. As microfabrication technology is based on silicon substrate, therefore silicon out-of-plane microneedles have been widely fabricated by the research community for TDD applications. Gardeniers et al. (2003) fabricated out-of-plane hollow microneedles with inclined structure. In the fabrication process, anisotropic etching of (111) plane was done in potassium hydroxide (KOH) wet etching. With the development of dry etching technology in silicon, Stoeber and Liepmann (2000) used dots arrays as a mask to fabricate hollow needles. In the fabrication

process, lumen was formed in DRIE and outside profile of needle was generated by isotropic wet & dry etching of silicon. Using the advanced ICP etching technology, Griss et al. (2003) developed side-opened microneedles, where outside shape of needle was fabricated by anisotropic and isotropic dry etching process with mask of cross pattern and inner channel was defined by DRIE on the backside of silicon substrate.

The microneedle design and analysis involves strength modelling and Computational fluid dynamics (CFD) analysis. Many research studies have been conducted for structural and microfluidic (flow) analysis of the microneedles. Shibata et al. (2007) conducted numerical and experimental studies for mechanical stability analysis of hollow cylindrical microneedle using silicon dioxide (SiO2) material. Wilke et al. (2005a, b) used numerical analysis for fluidic system to ensure uniform release of the fluid from each hollow microneedle. Aggarwal and Johnston (2004) used finite element (FE) analysis for prediction of various forces acting on the microneedle during skin insertion. Aoyagi et al. (2008) used finite element method (FEM) simulation and confirmed that the stress concentration occurred severely at the tip area of the microneedle and sharp tip angle of the microneedle could be easily inserted into skin. Paik et al. (2004) used in-plane single crystal silicon microneedle array for drug delivery and performed FEM simulation and experiments on microneedle for stress analysis by applying bending load at the tip of the microneedle. Stoeber and Liepmann (2002) developed syringe using MEMS technology and designed fluid mechanical model to avoid the clogging of the microneedle at inlet by increasing the internal diameter of the syringe in two steps. Stoeber and Liepmann (2002) performed CFD simulation using CFD ACE + Software to calculate shear rate in the flow for the appropriate scaling of the stepped internal lumen diameters. The study of fluidic system of the microneedle has also been done experimentally by many researchers (Griss et al. 2002, 2003; Gardeniers et al. 2003; Matteucci et al. 2008).

In our previous study we presented the design of a controlled drug delivery system for the treatment of cardiovascular or hemodynamic disorders such as hypertension (Nisar et al. 2008). In this work we present design and fabrication of hollow out-of-plane silicon microneedles to integrate with previously fabricated piezoelectrically actuated valveless micropump (Nisar et al. 2008). All the numerical studies reported in literature on the design and analysis of silicon microneedles cover either structural or fluid analysis only. In the present study, the authors have also performed both the structural and CFD analysis followed by coupled multified analysis of silicon microneedle based piezoelectrically actuated microfluidic device for the controlled drug delivery system. Since MEMS and

microfluidics are a new research area, hence there is a notable lack of applicable mathematical models and material information to predict fluid flow through micron sized silicon microneedle based piezoelectrically actuated microfluidic devices. That is why, numerical analysis involving structural, microfluidic and coupled multified analysis has been performed in the present study. The fabrication of silicon hollow microneedles is achieved by a series of combined isotropic and anisotropic etching processes using ICP etching technology. Then, an in-depth numerical analysis of a microneedle based piezoelectrically actuated microfluidic device is reported. The simulation involving transient multifield analysis using multiple code coupling method is conducted on a three dimensional model of the microneedle based microfluidic device. The multiple code coupling method involves sequential simulations consisting of piezoelectric analysis of piezoelectric actuator CFD analysis of fluid flow through the microneedles. The effect of voltage and frequency on piezoelectric/membrane deflection and fluid flow through the microneedles is investigated in the electro-fluid–solid coupled field analysis.

## Description of Drug Delivery System

The aim of this project is to design a microfluidic drug delivery device for treatment of cardiovascular disorder such as hypertension, etc. The main components of our system are electronic module, blood pressure sensor, flow sensor and drug delivery device. The block diagram of drug delivery system is shown in Fig. 2.

Electronic module provides the required circuitry. Blood pressure sensor in the system monitors patient's blood pressure. Based on the results of blood pressure sensor, the drug delivery system automatically injects the desired drug dose through the drug delivery device into patient's body. To insure the safety of patient the flow sensor accomplishes the real time sensing of release volume of drug. During the
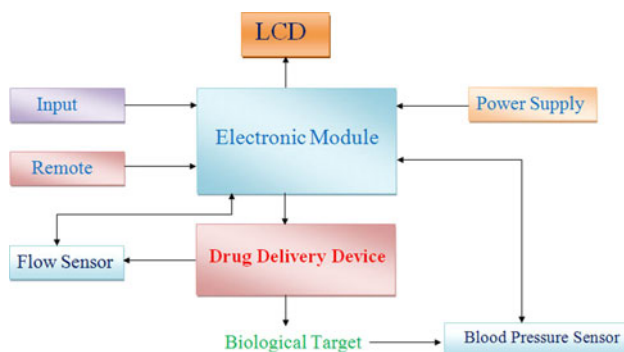
drug delivery, the flow is monitored by the flow sensors to prevent the large fluctuation of flow rate. Drug delivery device consists of piezoelectric actuator and a reservoir integrated with microneedle array. Actuator provides actuation mechanism to vibrate the membrane and reservoir integrated with microneedle array provides drug storage and interface between the drug delivery system and the patient's body for releasing the drug.

## Fabrication of Microneedles

The proposed fabrication process of microneedles and reservoir involves isotropic and anisotropic etching processes using standard silicon wafers. The desired shape of microneedle structures is achieved by controlling the etch times at various processing steps. The mask layout for hollow microneedles is shown in Fig. 3.

Three set of chrome masks were fabricated. Microneedle Mask MN1 has been used to fabricate microneedle outside shape. Microneedle mask MN2 has been used to fabricate inner hole called lumen while the third microneedle Mask MN3 has been used for backside reservoir etching. The fabrication process involves many steps. The deep reactive ion etching process parameters are shown in Table 2. The stepwise fabrication process of microneedles is shown in Fig. 4.

The first step involves wafer cleaning of single sided polished $6''$ Si wafer with Piranha solution and de-ionized (DI) water. The silicon wafer is then blown dry with air gun. The second step is to cap photoresist mask. This step involves various substeps such as spin coating photoresist AZ4620 @3000 rpm, soft bake (120–180 s @ 110°C, expose wafer, develop in developer solution AZ 400 K and hard bake. Then isotropic silicon dry etching of silicon wafer with ICP etch tool is done using $SF_6/O_2$ gases for outside shape of microneedle tips in standard photolithography process (etch depth = 15 μm). Then photoresist is stripped off and wafer is cleaned. The next step is to thermally grown silicon oxide layer on both sides of the wafer in oxidation furnace by wet oxidation at 1,000°C. Then each side of wafer is protected by capping with another wafer for mask oxide etching. Next step is to striped the photoresist. To perform first ICP etching, the photoresist is first coated with 5 μm thickness. The etching depth for first ICP etch is 150 μm. This is followed by second ICP etch up to 200 μm for backside reservoir etching. The front side is then capped and third ICP etching is done to make the reservoir on the backside of the wafer. The final steps involve release, oxide etch and dicing. The detailed fabrication steps are summarized in Table 3. The fabricated microneedles are shown in results and discussion section of the paper.



**Fig. 2** Block diagram of drug delivery system

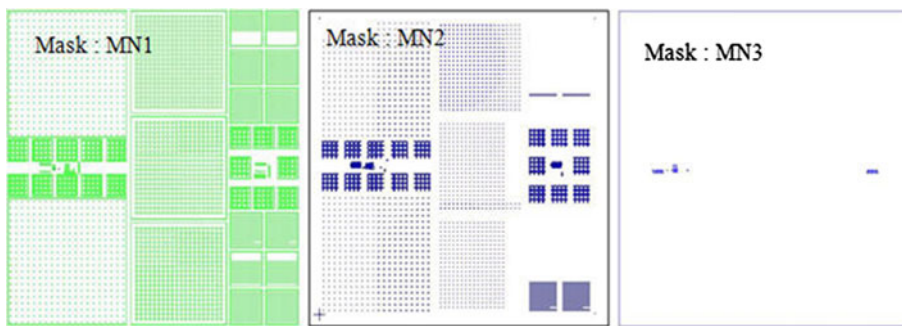**Fig. 3** Mask layout design of out-of-plane microneedles for fabrication

**Table 2** DRIE (Bosch process parameters)

| DRIE (Bosch process parameters) | Etching from front side | Etching from back side |
|---|---|---|
| Temperature (°C) | 15 | 20 |
| Etching time (min) | 15 | 25 |
| Stop time (min) | 3 | 3 |
| Power RF (W) | 1,400 | 1,600 |
| Etching/passivation | | |
| Flux $SF_6/C_4F_8$ (sccm) | 250/150 | 250/100 |
| Pressure $SF_6$ (Pa) | 3.5 | 4 |

## Analysis of Hollow Silicon Microneedles

### Mechanical Design

The microneedle design is cylindrical with tapered tip section, which provides enough strength and ease of skin insertion. The centre-to-centre distance of the microneedle in 5 × 5 microneedles array is 1,000 μm. The length of microneedle is limited to 200 μm to avoid contact of microneedle with sensory organs. The internal diameter (ID) is 60 μm and outer diameter (OD) is 150 μm. The fluid reservoir is designed on the backside of the microneedle. A schematic illustration of the design of microneedle with dimensions is shown in Fig. 5.

### Microfluidic Model Design

In this numerical study, two types of microfluidic analysis have been performed. First, CFD analysis is performed using static analysis with single phase and then, CFD analysis is performed using transient analysis with fluid–structure interaction. Figure 6 shows CFD model for single phase. For simplicity, single microneedle with drug reservoir is considered for the static analysis. One row of microneedle array with symmetry conditions is considered for transient multifield analysis (Fig. 11).

**Fig. 4** Fabrication process of hollow silicon out-of-plane microneedles
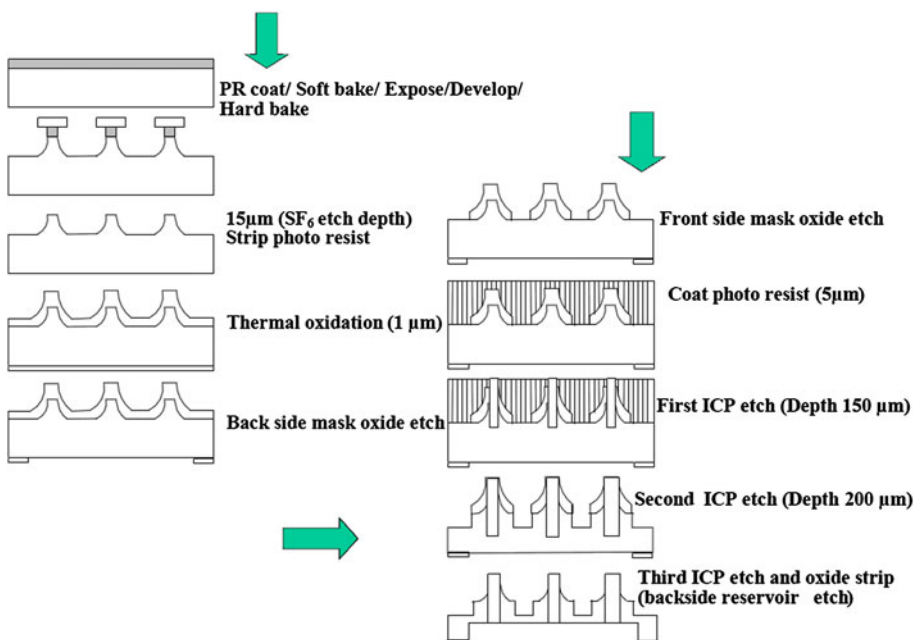
**Table 3** Microneedle fabrication process details

| Step no. | Process description | Stage | Equipment name | Remarks |
|---|---|---|---|---|
| 1 | Staring wafer | | | |
| 2 | Initial cleaning | Automatic wet bench | Automatic wet bench | Piranha + HF + SC-1 |
| 3 | PECVD oxide dep (backside) | PECVD_Oxide processes | Plasma enhanced chemical vapor deposition (PECVD) | 2 μm |
| 4 | Coating resist | Pattern photo-resist coat processes | Coater | |
| 5 | Exposure (aligner) | Expose processes done by Mask Aligner | Mask Aligner 1 | Microneedle mask MN3 (70 mJ/cm$^2$) |
| 6 | Development | Pattern photo-resist develop processes | Developer | Develop 75 s |
| 7 | Oxide backside etch | Silicon dioxide dry-etch processes | Reactive ion etching 1 | OXI-ETCH/2UM Develop 75 s |
| 8 | Oxide measurement | Thickness measurement processes | Ellipsometer | Ellipsometer < 50A |
| 9 | Wet resist strip | Strip_front | Manual acid wet bench | Piranha + HF + SC-1 (DI + Piranha + DI) |
| 10 | Ashing | Photo-resist ash processes | Hardened resist asher | Ashing |
| 11 | Wet resist strip | Front-end photo-resist wet strip | Manual acid wet bench | Piranha + HF + SC-1 (DI + Piranha + DI) |
| 12 | Cleaning | Front-end manual clean processes | Manual acid wet bench | DI + Piranha + DI |
| 13 | Coating resist | Pattern photo-resist coat processes | Coater | |
| 14 | Exposure (aligner) | Photo-resist expose processes done by Mask Aligner | Mask Aligner 1 | Microneedle MN1 (70 mJ/cm$^2$) |
| 15 | Development | Pattern photo-resist develop processes | Developer | Develop 75 s |
| 16 | Deep RIE (15 μm) | Poly-silicon dry-etch processes | Deep reactive ion etching | 15 μm |
| 17 | Wet resist strip | Front-end photo-resist wet strip | Manual acid wet bench | Piranha + HF + SC-1 (DI + Piranha + DI) |
| 18 | Ashing | Photo-resist ash processes | Hardened resist asher | Ashing |
| 19 | Wet resist strip | Front-end photo-resist wet strip | Manual acid wet bench | Piranha + HF + SC-1 (DI + Piranha + DI) |
| 20 | Cleaning | Front-end manual clean processes | Manual acid wet bench | DI + Piranha + DI |
| 21 | PECVD Oxide Dep | PECVD_Oxide processes | Plasma enhanced chemical vapor deposition (PECVD) | 2 μm |
| 22 | Oxide measurement | Thickness measurement processes | Ellipsometer | Ellipsometer 2 μm |
| 23 | Cleaning | Front-end manual clean processes | Manual acid wet bench | Anneal (700°C 30 min) |
| 24 | Anneal | Annealing processes done in AP furnaces | Anneal/drive-in furnace | Anneal (700°C 30 min) |
| 25 | Coating resist | Pattern photo-resist coat processes | Coater | |
| 26 | Exposure (aligner) | Photo-resist expose processes done by Mask Aligner | Mask Aligner 1 | Microneedle MN1 (70 mJ/cm$^2$) |
| 27 | Development | Pattern photo-resist develop processes | Developer | Develop 75 s |
| 28 | Oxide dry etch | Silicon dioxide dry-etch processes | Reactive ion etching 1 | OXI-Etch/2 μm |
| 29 | Oxide measurement | Thickness measurement processes | Ellipsometer | Ellipsometer < 50A |
| 30 | Wet resist strip | Front-end photo-resist wet strip | Manual acid wet bench | Piranha + HF + SC-1 (DI + Piranha + DI) |
| 31 | Ashing | Photo-resist ash processes | Hardened resist asher | Ashing |
| 32 | Wet resist strip | Front-end photo-resist wet strip | Manual acid wet bench | Piranha + HF + SC-1 (DI + Piranha + DI) |
| 33 | Cleaning | Front-end manual clean processes | Manual acid wet bench | DI + Piranha + DI |
| 34 | Coating Resist(5 μm) | Pattern photo-resist coat processes | Coater | Manual coat |
| 35 | Exposure (Aligner) | Photo-resist expose processes done by Mask Aligner | Mask Aligner 1 | Microneedle MN 2 (140 mJ/cm$^2$) |
| 36 | Development | Pattern photo-resist develop processes | Developer | Manual develop 2 min |

**Table 3** continued

| Step no. | Process description | Stage | Equipment name | Remarks |
|---|---|---|---|---|
| 37 | Oxide dry etch | Silicon dioxide dry-etch processes | Reactive ion etching 1 | OXI-Etch/2 μm |
| 38 | Oxide measurement | Thickness measurement processes | Ellipsometer | Ellipsometer < 50A |
| 39 | Deep RIE (150 μM) | Poly-silicon dry-etch processes | Deep reactive ion etching | Oxide 150 μm |
| 40 | Wet resist strip | Front-end photo-resist wet strip | Manual acid wet bench | Piranha + HF + SC-1 (DI + Piranha + DI) |
| 41 | Ashing | Photo-resist ash processes | Hardened resist asher | Ashing |
| 42 | Wet resist strip | Front-end photo-resist wet strip | Manual acid wet bench | Piranha + HF + SC-1 (DI + Piranha + DI) |
| 43 | Cleaning | Back-end manual clean processes | Manual acid wet bench | DI + Piranha + DI |
| 44 | Deep RIE (200 μm) | Poly-silicon dry-etch processes | Deep reactive ion etching | Oxide 200 μm |
| 45 | Deep RIE (300 μm) backside | Poly-silicon dry-etch processes | Deep reactive ion etching | Back grind 300 μm |
| 46 | Oxide wet etching | Wet-etch processes | Manual acid wet bench | Wet_etch < 50A |
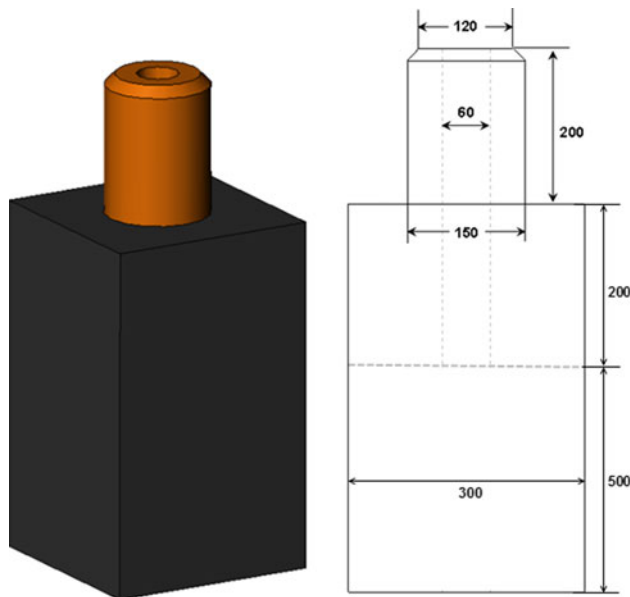


**Fig. 5** Design specification of hollow silicon microneedle (all dimensions are in μm)



**Fig. 6** CFD model using single code coupling

## Theoretical Analysis

The design of the cylindrical hollow silicon microneedle considered for strength modelling and CFD analysis is shown in Fig. 7.

$P1$ and $P2$ is the inlet and outlet pressure of the microneedle. $D1$ and $D2$ represent tip and outer diameter respectively. $L$ is the length of the microneedle and $Q$ is the flow rate in the lumen section.

### Microneedle Mechanics

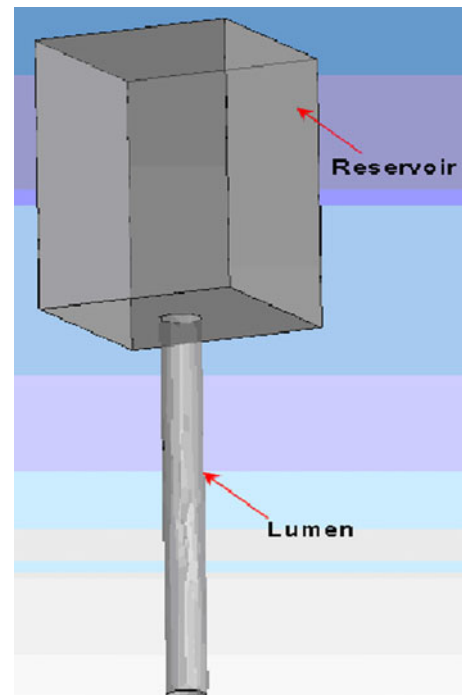During skin insertion, the possible failure of the microneedle may occur due to bending or buckling. An axial force acts on the microneedle tip during insertion. This axial force is compressive and causes buckling of the microneedle. The microneedle experiences resistive force exerted by skin during insertion, hence in order to pierce the microneedle into skin, the applied axial force has to be greater than skin resistance force. On the other hand, bending may occur due to uneven skin surface or human error during skin insertion. Hence, it is important to find the relation between microneedle geometry and mechanical properties of the material for proper microneedle design and to predict failure of the microneedle. The axial force
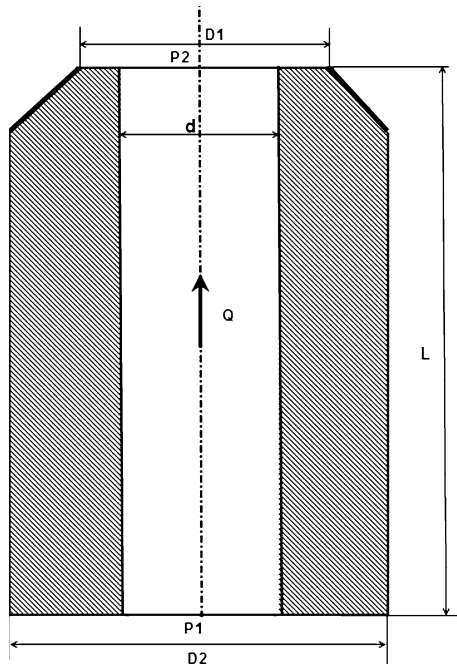
**Fig. 7** Cross section of the microneedle

(compressive force), which the microneedle can withstand without breaking is given by:

$$F_{\text{compressive}} = \sigma_y A \tag{1}$$

where, $\sigma_y$ is the yield strength of the material and $A$ is cross-sectional area of the microneedle tip.

The buckling force acting on the hollow microneedle during skin insertion is given by (Zahn et al. 2000; Gere and Timoshenko 1997)

$$B_{Buckling} = \frac{\pi^2 EI}{L^2} \tag{2}$$

where, $E$ is young's modulus of material; $I(m^4)$ is moment of inertia of cylindrical section and $L(m)$ is length of the microneedle.

Moment of inertia for hollow cylindrical section for Eq. 2 is $I = \frac{\pi}{64}(D^4 + d^4)$, where, $D$ is outer diameter and $d$ is inner diameter of hollow cylindrical section.

As microneedle penetrates the human skin, it experiences resistive forces exerted by the human skin. To penetrate the human skin, the outside force or pressure must be greater than the resistive skin force. The resistive force offered by the skin before punctured is given by the following equation:

$$F_{\text{resistance}} = P_{\text{pierce}} A \tag{3}$$

where, $P_{\text{pierce}}$ is the required pressure to pierce the microneedle into skin. As the microneedle penetrates the skin, the resistive force falls drastically (Frick et al. 2001). After the skin is pierced by the microneedle, the only force

that acts on the microneedle is the frictional force due to contact of tissue with the microneedle.

The bending force, which the microneedle can withstand without breaking is given by:

$$F_{\text{bending}} = \frac{\sigma_y I}{cL} \tag{4}$$

where, $c = \frac{D}{2}$ is the distance from vertical axis to the outer edge of the section (Aggarwal and Johnston 2004).

Microfluidic Analysis

It is important to model fluid flow characteristics because microneedles are used to inject drug solutions into skin. In hollow microneedles, the drug flows through the lumen thereby allowing increased drug transport. The pressure drop required in the microneedle for fluid flow is dependent on a number of factors such as microneedle geometry, fluid viscosity, and microneedle density. Microneedles have micronsized dimensions; therefore, there is significant resistance to flow. In designing of microneedles for TDD, measurements and predictions of fluid dynamics is important, so that the designed microneedle are small enough to avoid pain and yet sharp enough to penetrate into skin easily and large enough to achieve desired flow rate for drug delivery applications. To determine fluid flow through the microneedle, Poiseulle's law of fluid flow in a cylinder is considered:

$$Q = \frac{\pi(\nabla P)d^4}{128\mu(L)} \tag{5}$$

where, $d$ is the inner diameter of the microneedle and is constant throughout the lumen; $Q$ is the flow rate; $\nabla P$ is the pressure drop across the microneedle lumen; $\mu$ is the viscosity of fluid for water at 25°C; and $L$ is the length of the lumen of the microneedle.

The Reynolds number indicates the type of flow and is given as:

$$Re = \frac{\rho d V}{\mu} \tag{6}$$

where, $\rho$ is the density of fluid and is the fluid velocity in lumen.

At micron level, the flow becomes laminar. The flow is considered as laminar if is less than 2,100, otherwise the flow is considered as turbulent. The microneedle section shown in Fig. 5 is modelled by using Modified Bernoulli equation (Janna 1998). By considering the friction losses, the pressure loss by the fluid is calculated:

$$\frac{P_1}{\rho g} + \frac{V_1}{2g} + Z_1 = \frac{P_2}{\rho g} + \frac{V_2}{2g} + Z_2 + \frac{fL}{d} + \frac{V^2}{2g} + \sum \frac{kV^2}{2g} \tag{7}$$

where, $P_1$ is the inlet pressure; $P_2$ is the outlet pressure; $V_1$ is the inlet velocity; $V_2$ is the outlet velocity; $\rho$ is the

density of water; $Z_1$ and $Z_2$ is the distances from datum ($Z_1 = 0$ and $Z_2 = L$); $f$ is the friction factor.

The pressure drop can be calculated from Eq. 8:

$$\nabla P = \mu \frac{128Q(L)}{\pi d^4} + \rho \frac{8Q^2}{\pi^2 d^2}(k) \qquad (8)$$

where, $k$ is the loss coefficient factor for the square edge inlet and outlet. The value of loss coefficient for the microneedle design is taken as 0.5. The friction factor for laminar flow is given a $f = \frac{64}{Re}$ (Janna 1998). The first term of right hand side in Eq. 8 describes the pressure drop due to viscous shear force (Batchelor 1967) and second term describes inertial effect at the inlet and exit (Stoeber and Liepmann (2000)).

## Piezoelectric Analysis

Piezoelectric analysis involves coupling of structural and electric fields. When a voltage is applied to the piezoelectric material, the piezoelectric material exhibits deformation and conversely a vibrating piezoelectric material generates voltage. The effectiveness of mechanical to electrical energy and vice versa can be expressed by the electromechanical conversion factor $k'$.

$$k' = \frac{\text{output of electrical energy}}{\text{input of mechanical energy}} \qquad (9)$$

The actuator consists of piezo disk that is attached with silicon membrane. The displacement of the actuator is small enough that all materials are in their linear elastic limits. By the theory of piezoelectricity, the stress $T_r^P$ is caused around the circumference of piezoelectric actuator and remains the same along the thickness direction.

$$T_r^P = -\frac{Ed'V_0}{(1-\sigma)h} \qquad (10)$$

where, $d'$ is the piezoelectric coupling coefficient.

The matrix form of the simultaneous full coupling applicable to piezoelectric actuators is:

$$\begin{bmatrix} [K_{11}] & [K_{12}] \\ [K_{21}] & [K_{22}] \end{bmatrix} \begin{Bmatrix} \{X_1\} \\ \{X_2\} \end{Bmatrix} = \begin{Bmatrix} \{F_1\} \\ \{F_2\} \end{Bmatrix} \qquad (11)$$

where, $[K_{i,j}]$; $i, j = 1, 2$ are stiffness sub-matrices; $[F_i]$; $i = 1, 2$ are force vector;$[X_i]$; $i, j = 1, 2$ are two types of degree of freedom.

The off-diagonal sub-matrices $[K_{12}]$ and $[K_{21}]$ account for the coupling effect. The equations of elasticity are coupled to the charge equation of electrostatics by means of piezoelectric constants in linear piezoelectric analysis ANSI/IEEE Std 176 (1987):

$$\begin{Bmatrix} [T] \\ [D] \end{Bmatrix} = \begin{bmatrix} [c]^E & [e] \\ [e]^T & [\varepsilon] \end{bmatrix} \begin{Bmatrix} [S] \\ [-E] \end{Bmatrix} \qquad (12)$$

where, $[T] = $ stress vector, $[D] = $ electric flux density vector; $[S] = $ strain vector, $[E] = $ electric field vector,

$[c]^E = $ elasticity matrix evaluated at constant electric field, $[e] = $ piezoelectric stress matrix, $[e]^T = $ dielectric matrix at constant strain.

## Multifield Analysis

In this paper, an in-depth multifield analysis of a microneedle based piezoelectrically actuated microfluidic device with integrated drug reservoir and microneedle array is presented. When excitation voltage is applied on the piezoelectric actuator, the attached silicon membrane to the piezoelectric actuator deforms in upward or downward direction depending on the polarity of the applied voltage. The application of voltage to the piezoelectric actuator generates periodic excitation force ($f$), which deforms the silicon membrane periodically thus generating fluid flow to and from the chamber. The vibration of the membrane is described through the change of its displacement or the deflection '$W_P$' with respect to time and space. Mostly the deflection of the membrane with respect to the membrane length is very small. Therefore the bending theory of the plates is applicable and the deflection '$W_P$' of the membrane is given as (Fan et al. 2005; Timoshenko and Krienger Woinowsky 1995):

$$D\nabla^4 W_P + \rho h \frac{\partial^2 W_P}{\partial t^2} = f - P \qquad (13)$$

where,

$$D = \frac{Eh^3}{12(1-v^2)}$$

($E = $ modulus of elasticity; $h = $ membrane thickness; $v = $ Poisson ratio)

$F$      actuating force generated by membrane
$P$      dynamic pressure imposed on the membrane by the fluid
$\rho_P$      density of the Membrane
$\nabla^4$      two dimensional double Laplacian operator

## Numerical Simulation

### Structural Analysis

The structural analysis of the microneedle is performed using FEM. During skin insertion, microneedle experiences axial force, bending force, shear force etc. Single out-of-plane microneedle was modelled with fixed base and free tip end for the bending and axial stress analysis. The structural model was built by using element SOLID186, which is mostly used to model silicon material. Linear isotropic material properties of silicon were used for FEM

**Fig. 8** Bending stress analysis
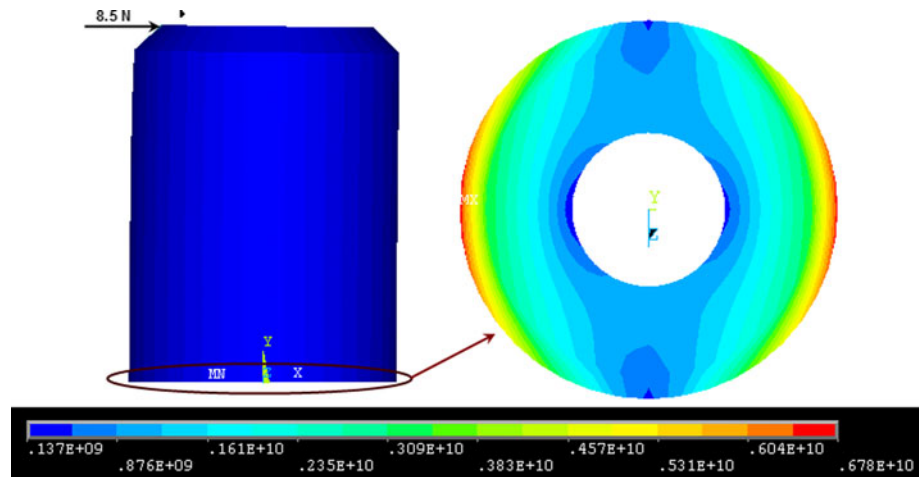


analysis (Young's modulus of 169 GPa with Poisson ratio of 0.22 and fracture strength of 7 GPa were considered (Aggarwal and Johnston 2004). In the simulation study, bending and axial stress analysis was performed by applying transverse and axial loads respectively. The range of transverse load is assumed according to the fracture strength of the material. For the microneedle failure analysis, stress at the fixed end (bottom) of the microneedle was taken into consideration. Figure 8 shows the simulation result at the bottom of the microneedle for the applied bending force at the tip.

It was found in the numerical solution that the maximum stress of 6.78 GPa occurs at the bottom of the microneedle for the applied bending force of 8.5 N, which is below the yield strength of the material. The skin offers resistance of 3.18 MPa (Wilke et al. 2005a, b; Wang et al. 2006) during microneedle penetration into human skin. Hence, to overcome this skin resistance, the microneedle must withstand the load more than 3.18 MPa. Hence, to show the effect of this resistance force on the structure of the microneedle, FEM analysis was performed. The effect of applied axial load on the free end of the microneedle is shown in Fig. 9.
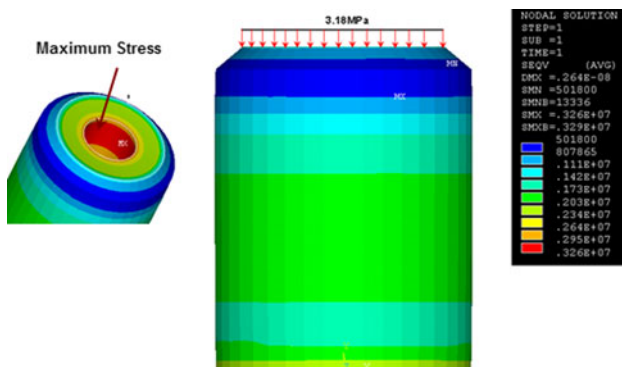


**Fig. 9** Axial stress analysis

The maximum stress occurs inside the lumen section of the microneedle, which is well below the yield strength limit with negligible deflection. The result shows that the microneedle design is strong enough to penetrate into the human skin without failure.

CFD Analysis

This study shows the effect of different inlet pressures on the flow rate. CFD analysis was conducted to predict the flow rate and pressure drop of the fluid flowing through the microneedle. CFD analysis is done by using two different simulations for flow rate analysis. In the first simulation, the static pressures were applied at the inlet of the microneedle reservoir. In the second type of simulation, transient analysis was performed using multiple code coupling.

*CFD Analysis at Different Inlet Pressures*

In this analysis, the simulation is done by applying static pressures of 20–100 kPa at the inlet of the microneedle. The available micropumping devices in the market provide the outlet pressure between 10 and 100 kPa (Khumpuang et al. 2003) which can be easily integrated with microneedle array for drug delivery applications. For the simulation, water at 25°C was modelled as an isothermal fluid domain. The simulation results for the applied inlet static pressure are shown in Fig. 10.

The pressure of 20–100 kPa was applied at the inlet of the microneedle. The outlet pressure was assumed to be 0 kPa because the previous study (Khumpuang et al. 2003) showed negligible pressure at the outlet of the microneedle. The simulation result shows that the velocity of the fluid is negligible in the reservoir zone due to large area but the velocity increases in the microneedle lumen section and again increases along the length due to small area. Due to frictional losses between fluid and wall, the velocity of the
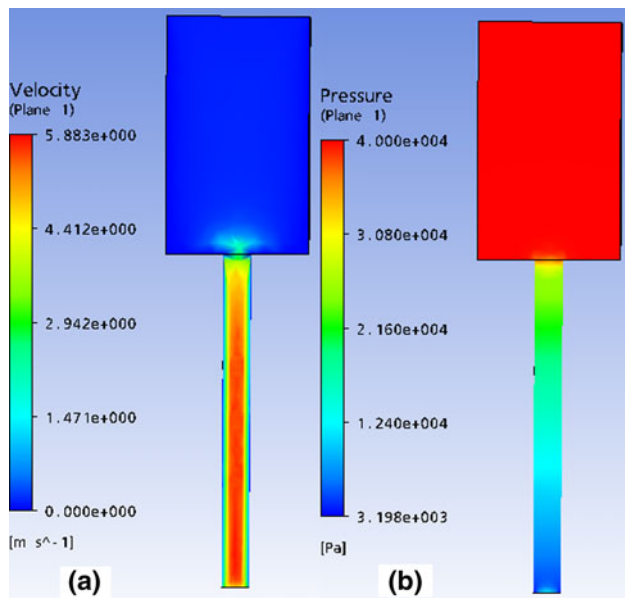
**Fig. 10** **a** 2D view of the microneedle for velocity distribution using CFD analysis. **b** 2D view of the microneedle for pressure distribution using CFD analysis

fluid is less at the wall area of the lumen as compared to the central region of the lumen section.

*CFD Analysis Using Transient Multifield Code Coupling*

For the electromechanical coupling of piezoelectric actuator and fluid-membrane coupling, the multifield analysis using multiple code coupling has been conducted in ANSYS. Multifield analysis involves fluid–structure coupling, in which structural model sends surface load to the fluid model. At the same time fluid model sends forces to the structural model during the simulation. The fluidic model of piezoelectrically actuated drug delivery device is shown in Fig. 11.

The sequential method was used for ANSYS and CFX field analysis, where ANSYS field was solved initially. The fluid solid interface (FSI) was defined using FS command with FSI surface load label. The FSI surface is created in CFX model with same name for the proper communication
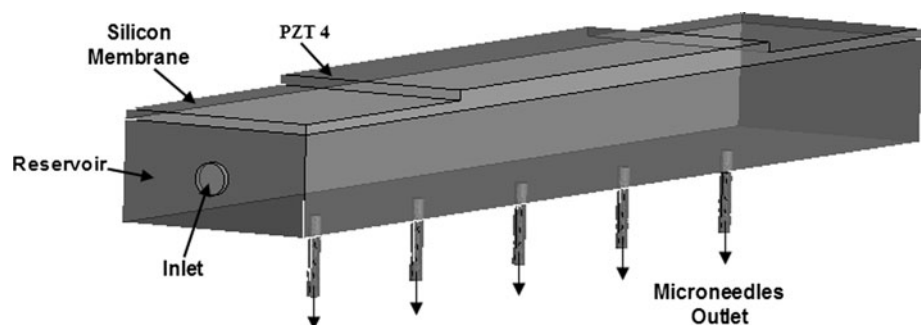
between ANSYS and CFX solver. The Multifield simulation results were obtained using MFX-ANSYS/CFX simulation environment. ANSYS coupled field element SOLID-226 with displacement and voltage degrees of freedom has been used for piezoelectric material. SOLID-95 element is used for silicon membrane. For this analysis, water at 25°C was assumed as an isothermal fluid domain. The material properties of the PZT4 and silicon materials are given in Table 4.

For transient analysis, circuit element CIRCU-94 has been used. The thickness of the piezoelectric and silicon membrane is 100 μm. Only one row of microneedle array is considered for the simulation due to symmetry condition. The model boundary conditions for the fluid–structure interface are shown in Fig. 12.

## Results and Discussion

### Fabrication of Microneedles

Microneedles with high aspect ratio have been fabricated using a series of combined isotropic and anisotropic etching processes in ICP etching machine. Wet etching was used for front and back side mask oxide etching. The microneedle tip was fabricated by isotropic etching using $SF_6/O_2$ gases in inductively coupled plasma etcher. The BOSCH process was used for outer vertical shape, lumen and backside etching. The scanning electron microscope (SEM) images of the fabricated microneedles are shown in Fig. 13.

### Stress Analysis

The stress analysis of the designed microneedle is done in the first set of the simulation. The deflection and stress of the microneedle is measured for the applied transverse force and is depicted in Fig. 14.

The microneedle fails if the stress value exceeds the yield strength of the material. For the applied bending force of 8.5 N at the tip, the maximum stress at the bottom of the microneedle is found to be 6.78 GPa with deflection of

**Fig. 11** CFD model for coupled multifield analysis

**Table 4** Material properties

| Material | Properties | Value | | |
|---|---|---|---|---|
| Piezoelectric (PZT-4) (Analysis Guide, ANSYS Release 11.0) | Density (Kg/m$^3$) | 7500 | | |
| | Elasticity stiffness matrix (N/m$^2$) | $\begin{bmatrix} 13.2 & 7.3 & 7.1 & 0 & 0 & 0 \\ 7.3 & 11.5 & 7.3 & 0 & 0 & 0 \\ 7.1 & 7.3 & 13.2 & 0 & 0 & 0 \\ 0 & 0 & 0 & 2.6 & 0 & 0 \\ 0 & 0 & 0 & 0 & 2.6 & 0 \\ 0 & 0 & 0 & 0 & 0 & 3 \end{bmatrix} \times 10^{10}$ | | |
| | Piezoelectric stress matrix (C/m$^2$) | $\begin{bmatrix} 0 & -4.1 & 0 \\ 0 & 14.1 & 0 \\ 0 & -4.1 & 0 \\ 10.5 & 0 & 0 \\ 0 & 0 & 10.5 \\ 0 & 0 & 0 \end{bmatrix}$ | | |
| | Permittivity | $x$ | | 804.6 |
| | | $y$ | | 659.7 |
| | | $z$ | | 804.6 |
| Silicon (Si) (Cui et al. 2007) | Young's modulus (N/m$^2$) | $168.9 \times 10^9$ | | |
| | Density (kg/m$^3$) | 2329 | | |
| | Poisson's ratio | 0.3 | | |



**Fig. 12** Modal boundary conditions
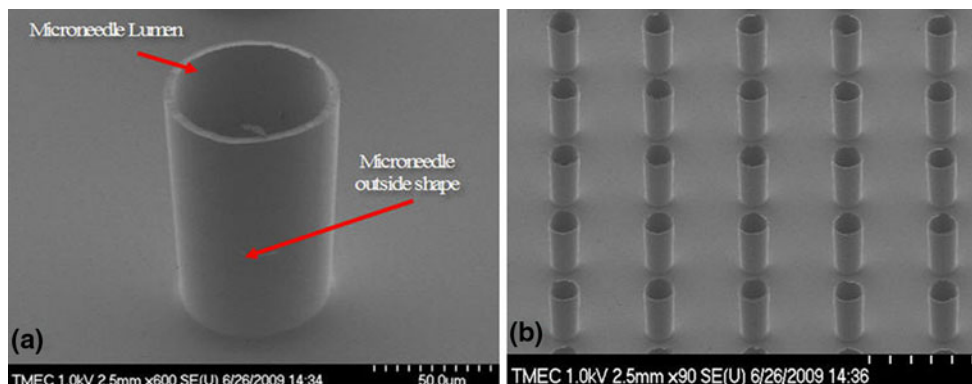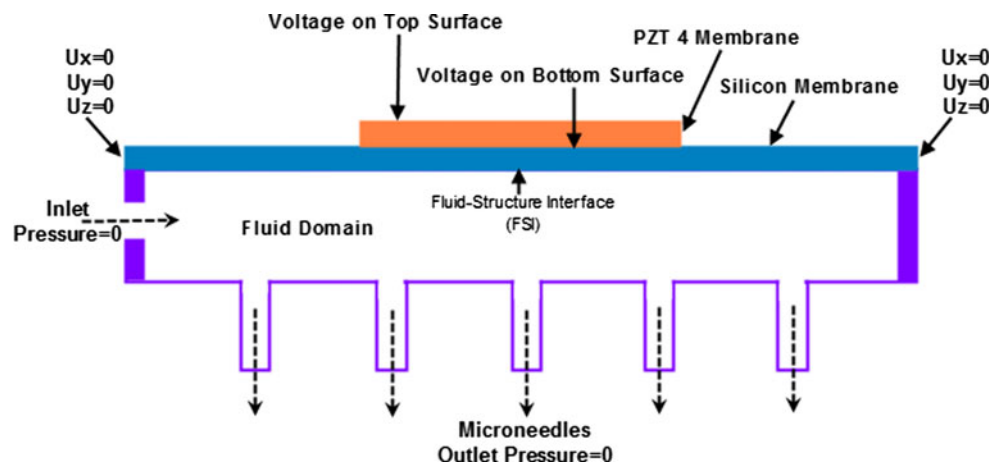


**Fig. 13** SEM images of the fabricated microneedle array

**Fig. 14** Variation in stress and deflection of microneedle for applied force
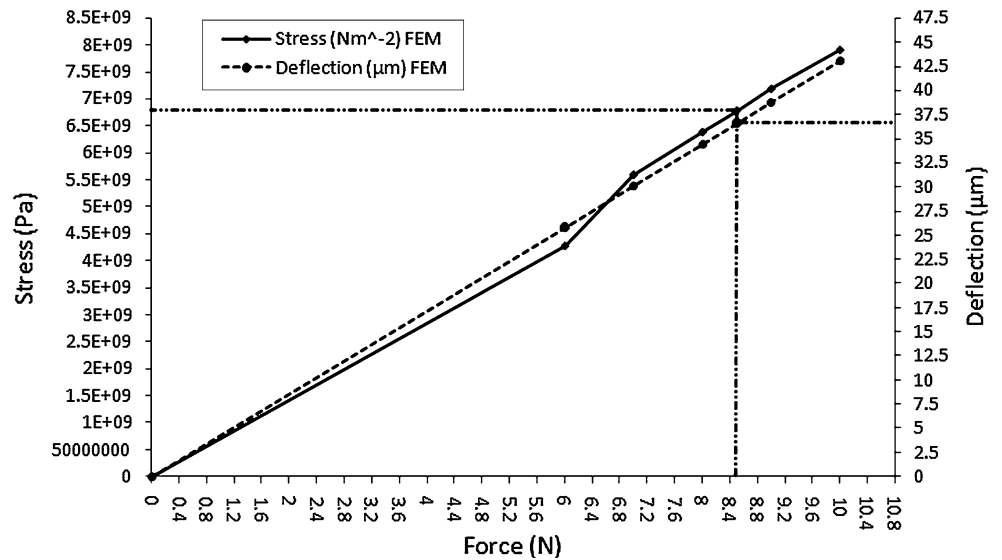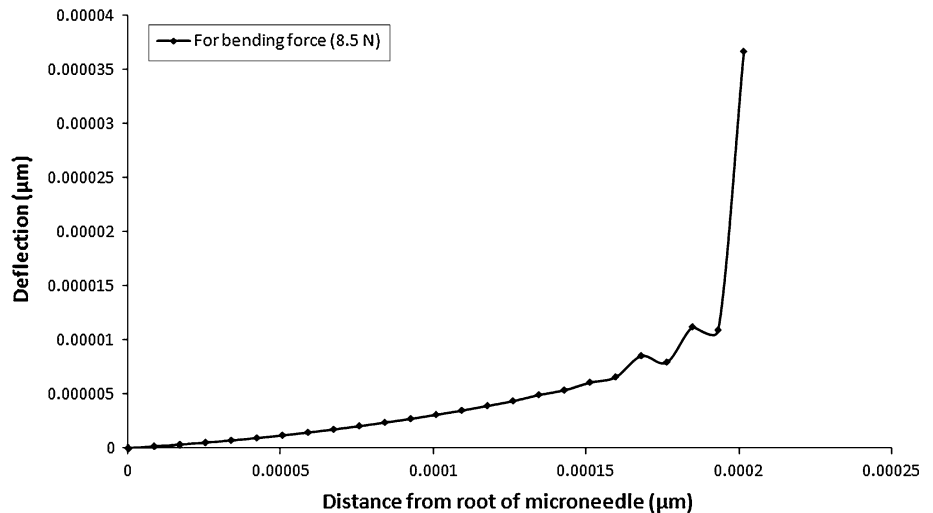


**Fig. 15** Deflection of the microneedle along its length due to applied bending force



36.6 μm. As the stress is below the yield stress (7 GPa) of the material hence, the microneedle is able to withstand the force of 8.5 N. The designed microneedle is strong due to its cylindrical section. The deflection of the microneedle along its length is shown in Fig. 15.

The deflection of the microneedle gradually increases with increase in distance from root of the microneedle. As the bending force is applied directly at the microneedle tip, therefore maximum deflection occurs at the tip of the microneedle. The main focus of the study is also to determine overall microneedle structure strength and to predict deflection on the rest of the microneedle section other than the tip. During microneedle insertion, skin offers resistance to the microneedle due to its elastic property. During the skin insertion microneedle should not damage. Hence, it is important to analyse the behaviour of the microneedle during skin insertion. The microneedle can

puncture the human skin with applied skin piercing pressure of 3.18 MPa (Wilke et al. 2005a, b; Wang et al. 2006) at the tip of the microneedle without failure. For the applied skin piercing pressure, the maximum stress of 3.26 MPa with negligible deflection was found in the lumen area, which is less than yield stress of the material. From the above results, it is predicted that the proposed microneedle design can withstand the bending as well as axial forces during skin insertion.

## Flow Analysis for Applied Static Pressure

The flow rate at various applied pressures is shown in Fig. 16. The flow rate increases with the increase in inlet pressure. The maximum flow rate recorded is 1,050 μl/min at 100 kPa.

**Fig. 16** Flow rate for the applied static pressure at inlet of the reservoir
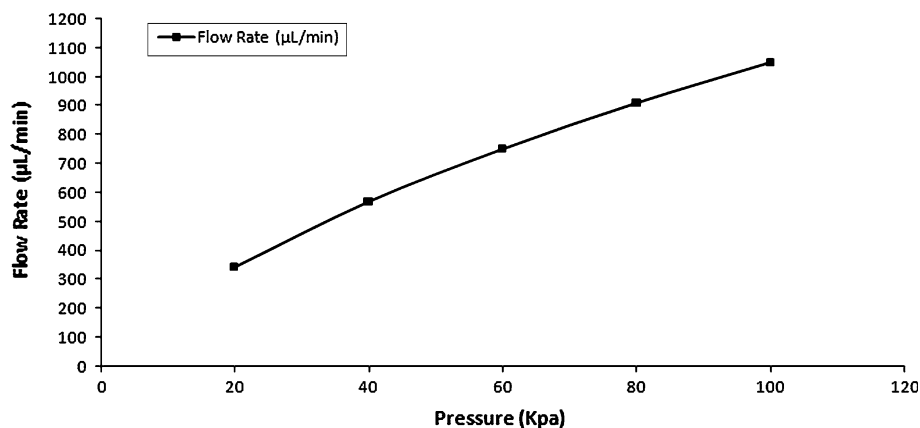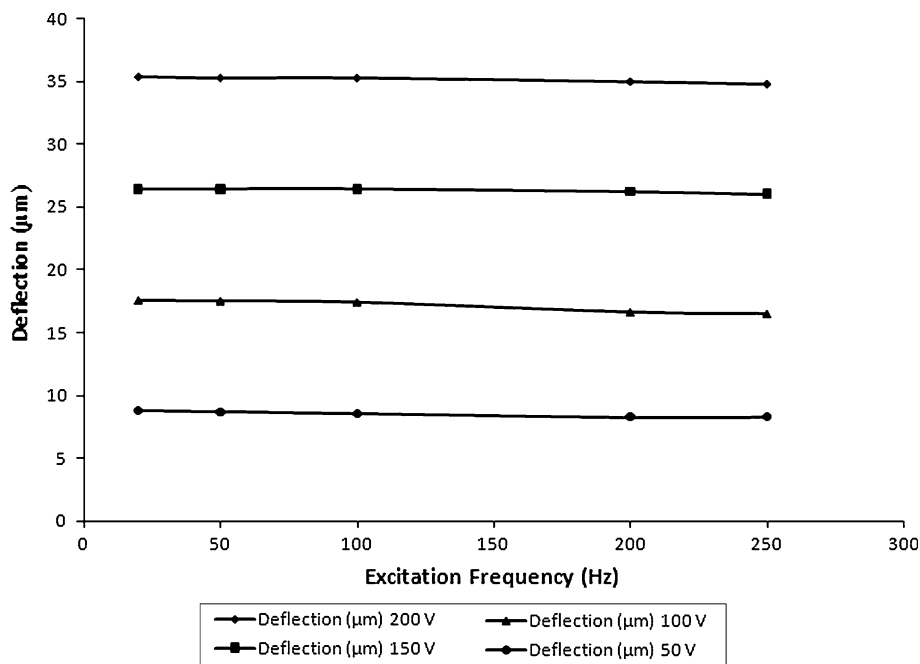


**Fig. 17** Deflection of the piezoelectric actuator at various excitation voltages



## Transient Multifield Analysis

Figure 17 shows the relationship between piezoelectric membrane deflection and excitation frequency for different excitation voltages. The membrane deflection increases with increase in excitation voltage but slowly decreases with increase in excitation frequency at the same voltage. The deflection of the piezoelectric membrane is strongly affected by excitation voltage but not effected by varying excitation frequency if varied from 20 to 250 Hz.

The variation in flow rate with the excitation frequency for different excitation voltages is shown in Fig. 18.

The flow rate increases gradually with increase in excitation frequency. The maximum flow rate is obtained at 100 V and it increases with the excitation frequency. The simulation results show that the maximum flow rate is

not at the maximum deflection of the membrane as reported previously (Guo et al. 2007; Jang et al. 2007). Various researchers (Nguyen et al. 2002; Guo et al. 2007; Jang et al. 2007; Izzo et al. 2007) have shown the effect of frequencies on the flow rate. Most of the results show that the flow rate of the micropump initially increases with increase in frequency and after a certain value of frequency the flow rate decreases or remain unchanged. The simulation results in Fig. 19 show that the flow rate is maximum at low voltages than at high voltages.

The variation in flow rate with frequency is also dependent upon the material properties of the pump membrane as well as piezoelectric/membrane thickness. For the current design of piezoelectric actuator, maximum flow of 83.99 μl/min is obtained through the microneedle array at maximum frequency of 250 Hz at 100 V with deflection of 16.48 μm.

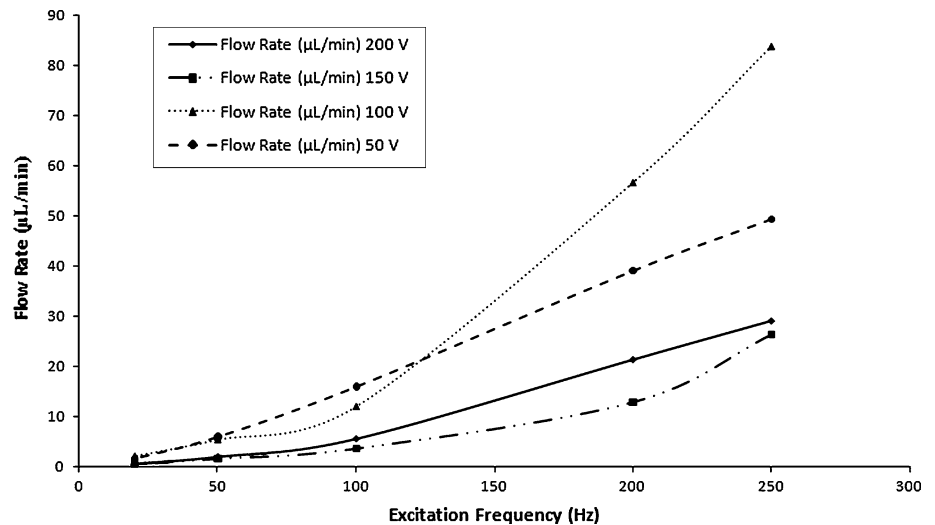**Fig. 18** Effect of excitation frequencies on flow rates at the different excitation voltages
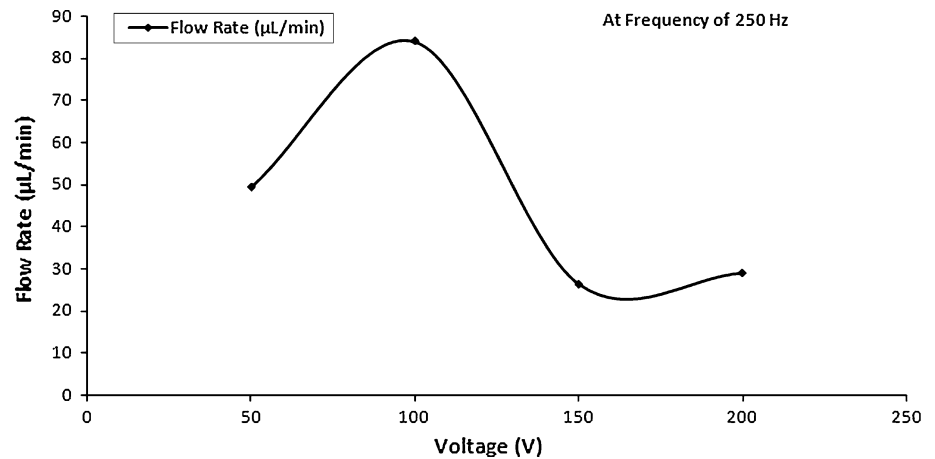


**Fig. 19** Effect of different excitation voltages on flow rates



## Pulsatile Drug Delivery and Microfluidic Device Efficiency

Controlled delivery devices are increasingly being developed as these systems deliver the right dose at specific drug time and specific site. Such devices have made it possible to meet critical medical needs such as nearly constant drug level at the site of action, prevention of peak-valley fluctuations, site specific drug delivery, reduced side effects and increased therapeutic effectiveness. However, there are certain medical conditions for which constant drug release pattern is not suitable. These conditions demand release of drug after a delay time. Such a release pattern is known as pulsatile release (Bussemer et al. 2001). Study of pulsatile flow is extremely important at the small scales in microdevices because the flow of blood is pulsatile rather than steady. Recent research has shown that some diseases have a predictable cyclic rhythm and that the timing of drug release can significantly improve the outcome of a desired

effect (Bussemer et al. 2001). This condition requires release of drug as a "pulse" after a time delay. Glasgow et al. (2004a, b) reported that the nature of flow affects the degree of mixing and the intermediate flows have a higher degree of mixing as compared to quasi-steady flows. The governing equation for pulsatile flow is given by (Yakhot et al. 1999):

$$\frac{\partial V}{\partial t} = -\frac{1}{\rho}\frac{\partial \tilde{p}}{\partial x} + \alpha \nabla^2 V \tag{14}$$

where, $V$ is the velocity profile, $\rho$ is fluid density, and $\tilde{P}$ is pulsatile pressure.

Some of the diseases where pulsatile drug delivery devices are promising include duodenal ulcer, cardiovascular diseases, arthritis, asthma, diabetes, neurological disorder, cancer, hypertension and hypercholesterolemia. Using MEMS technology, complex drug release patterns (such as simultaneous constant and pulsatile release) can be achieved using the microchip integrated with MEMS based

microfluidic devices. Such MEMS based devices have the ability to control both release time and release rate. The proposed drug delivery system as depicted in Fig. 2 also aims at developing a pulsatile drug delivery system for treatment of hemodynamic dysfunctions such as hypertension. The velocity fields, pressure and flow patterns in the proposed MEMS based piezoelectrically actuated integrated microfluidic device with microneedles are pulsatile in nature. Therefore, such systems have a great potential towards treating such disease conditions such as hypertension which require drug release as pulse after a time delay.

It is also worth mentioning here that pulsatile velocity fields and the unsteadiness of the flow may affect the performance of the microfluidic devices such as the one described in this paper. However, the efficiency of microfluidic devices is almost frequency independent at very low frequencies (Sun and Huang, 2006; Ahmadian et al. 2006). This is due to the fact that when the excitation frequency is very low compared to the natural frequency of the piezoelectric actuator (typically in MHz in case of piezoelectric actuation), the nonlinear effects of the electro-fluid structural coupling at zero pump pressure are negligible. Therefore, steady flow analysis of microfluidic devices may be used for the design of piezoelectrically actuated microfluidic devices with integrated microneedles at low frequencies. Wang et al. (2007) concluded that the driving frequency and the net volume flow are the two most important parameters in studying the efficiency of the microfluidic devices such as micropump. Yao et al. (2007) found that net flow rate increased rapidly with increasing frequency, and reached the peak at frequency of 250 Hz, then decreased slowly with further increase in frequency. Coupled multifield analysis of the integrated piezoelectrically actuated microfluidic device in the present study shows the effects of excitation frequency and voltage on piezoelectric membrane deflection and flow rate through the microneedles. The results show that flow rate through the microfluidic device increases with increase in excitation frequency as shown in Fig. 18. It is also shown that maximum flow rate occurs at lower voltages as compared to higher voltages for a particular frequency as shown in Fig. 19.

## Conclusion

In this work, fabrication of silicon hollow microneedles involving ICP technology is first presented for TDD system for the treatment of cardiovascular or hemodynamic disorders such as hypertension. Then, a numerical study using multiple code coupling method is conducted on a three dimensional model of the silicon microneedle based microfluidic device with piezoelectric actuator. Using a combination of isotropic and an isotropic and anisotropic

etching processes, microneedle designs with ID = 60 μm, OD = 150 μm center-to-center spacing = 1,000 μm were successfully fabricated. The simulated results show that at the applied skin piercing pressure of 3.18 MPa, the maximum stress of 3.26 MPa with negligible deflection was found in the lumen area of the silicon microneedle, which is less than yield stress of the material. Numerically predicted results show that the proposed microneedle design can withstand the bending as well as axial forces during skin insertion. Coupled multified analysis of microneedle based piezoelectrically actuated device shows that piezoelectric-membrane assembly deflection increases with increase in excitation voltage but slowly decreases with increase in excitation frequency at the same voltage. The deflection of the piezoelectric-membrane assembly is strongly affected by excitation voltage but not effected by varying excitation frequency if varied from 20 to 250 Hz. Maximum flow rate of microneedle based piezoelectrically actuated device does not occur at maximum deflection of the membrane. For the current design of piezoelectric actuator with integrated microneedles, maximum flow of 83.99 μl/min is obtained at maximum frequency of 250 Hz at 100 V with deflection of 16.48 μm. The velocity fields, pressure and flow patterns in the proposed MEMS based piezoelectrically actuated integrated microfluidic device with microneedles are pulsatile in nature. Therefore, such systems are effective towards treating such disease conditions such as hypertension which require pulsatile drug release profile. The fabricated microneedles can be integrated with our previously fabricated piezoelectric valveless micropump. In future work, experimental characterization of the microneedle array patch integrated with piezoelectrically actuated microfluidic device will be conducted. The results of integrated system will be presented in the subsequent paper.

## References

Aggarwal P, Johnston CR. Geometrical effects in mechanical characterizing of microneedle for biomedical applications. Sens Actuators B. 2004;102:226–34.

Ahmadian M, Saidi M, Mehrabian A, Bazargan M, Kenarsari S. Performance of valveless diffuser micropumps under harmonic piezoelectric actuation. In: ASME conference on engineering systems design and analysis. 2006.

ANSI/IEEE Std 176. IEEE standard on piezoelectricity. IEEE; 1987. http://standards.ieee.org/reading/ieee/std_public/description/ultrasonics/176-1987_desc.html.

Aoyagi S, et al. Biodegradable polymer needle with various tip angles and consideration on insertion mechanism of mosquito's proboscis. Sens Actuators A. 2008;143:20–8.

Arora A, Prausnitzc MR, et al. Micro-scale devices for transdermal drug delivery. Int J Pharm. 2008;364:227–36.

Barry BW. Novel mechanisms and devices to enable successful transdermal drug delivery. Eur J Pharm Sci. 2001;14:101–14.

Batchelor GK. An introduction to fluid dynamics. University of Cambridge. 1967.

BeMent SL, et al. Solid-state electrodes for multichannel multiplexed intracortical neuronal recording. IEEE Trans Biomed Eng. 1986;33(2):230–41.

Bodhale DW, Nisar A, Afzulpurkar N. Structural and microfluidic analysis of hollow side-open polymeric microneedles for transdermal drug delivery applications. Microfluid Nanofluid. 2009. doi:10.1007/s10404-009-0467-9.

Brown MB, Martin GP, et al. Dermal and transdermal drug delivery systems: current and future prospects. Drug Deliv. 2006;13: 175–87.

Bussemer T, Otto I, Bodmeier R. Pulsatile drug delivery systems. Crit Rev Ther Drug Carrier Syst. 2001;18(5):433–58.

Campbell PK, et al. A silicon-based, three-dimensional neural interface: manufacturing processes for an intracortical electrode array. IEEE Trans Biomed Eng. 1991;38(8):758–68.

Chen J, et al. A multichannel neural probe for selective chemical delivery at the cellular level. IEEE Trans Biomed Eng. 1997;44(8):760–9.

Cui Q, Liu C, Xuan F. Study on a piezoelectric micropump for the controlled drug delivery system. Microfluid Nanofluidics. 2007;3(4):377–90.

Fan B, Song G, Hussain F. Simulation of piezoelectrically actuated valveless micropump. J Smart Mater Struct. 2005;14:400–5.

Frick TB, et al. Resistance forces acting on suture needles. J Biomech. 2001;34:1335–40.

Gardeniers HJGE, et al. Silicon micromachined hollow microneedles for transdermal liquid transport. J Microelectromech Syst. 2003;12(6).

Gere J, Timoshenko S. Mechanics of materials, 4th edn. 1997.

Glasgow I, Lieber S, Aubry N. Parameters influencing pulsed flow mixing in microchannels. Anal Chem. 2004a;76:4825–32.

Glasgow I, Batton J, Aubry N. Electroosmotic mixing in microchannels. Lab Chip. 2004b;4:558–62.

Griss P, Enoksson P, Tolvanen Laakso HK, Merilainen P, Ollmar S, Stemme G. Micromachined electrodes for biopotential measurements. IEEE ASME J Microelectromech Syst. 2001;10(1):10–6.

Griss P, Tolvanen Laakso H, Merilainen P, Stemme G. Characterization of micromachined spiked biopotential electrodes. IEEE Trans Biomed Eng. 2002;49(6):597–604.

Griss P, et al. Side-opened out of plane microneedles for microfluidics transdermal liquid transfer. J Microelectromech Syst. 2003; 12(3):296–301.

Guo SX, Pei Z, Wang T, Ye XF. A novel type of pulseless output micropump based on magnet-solenoid actuator. In: IEEE/ICME international conference on complex medical engineering. 2007. p. 96–100.

Henry S, et al. Micro machined needles for the transdermal drug delivery of drugs. In: Proceedings of IEEE workshop MEMS. 1998. p. 494–98.

Izzo I, Accoto D, Menciassi A, Schmitt L, Dario P. Modelling and experimental validation of a piezoelectric micropump with novel no-moving-part valves. Sens Actuators A. 2007;133:128–40.

Jang LS, Li YJ, Lin SJ, Hsu YC, Yao WS, Tsai MC. A stand-alone peristaltic micropump based on piezoelectric actuation. Biomed Microdevices. 2007;9(2):185–94.

Janna WS. Design of fluid thermal system. 2nd ed. Boston: PWS Pub.; 1998.

Karande P, Jain A, et al. Discovery of transdermal penetration enhancers by high-throughput screening. Nat Biotechnol. 2004; 22:192–7.

Khumpuang S, et al. Design and fabrication of coupled microneedle array and insertion guide array for safe penetration through skin. In: International symposium of micromechatronics and human science. 2003.

Kim K, Park D, Lu H, Kim K-H, Lee JB. A tapered hollow metallic microneedle array using backside exposure of SU-8. J Micromech Microeng. 2004;14:597–603.

Matteucci M, et al. A compact and disposable transdermal drug delivery system. Sincrotrone Trieste, I-34012 Basovizza-Trieste, Italy. 2008.

Moon SJ, Lee SS. A novel fabrication method of a microneedle array using inclined deep x-ray exposure. J Micromech Microeng. 2005;15:903–11.

Mukherjee EV, et al. Microneedle array for transdermal biological fluid extraction and in situ analysis. Sens Actuators A. 2004;114:267–75.

Nguyen NT, Huang XY, Chuan TK. MEMS-micropumps: a review. J Fluids Eng Trans ASME. 2002;124(2):384–92.

Nisar A, Afzulpurkar N, Tuantranont A, Mahaisavariya B. Three dimensional transient multifield analysis of a piezoelectric micropump for drug delivery system for treatment of hemodynamic dysfunctions. Cardiovasc Eng. 2008;8(4):203–18.

Oka K, Aoyagi S, Arai Y, Isono Y, Hashiguchi G, Fujita H. Fabrication of a microneedle for a trace blood test. Sens Actuators A. 2002;97–98:478–85.

Paik SJ, et al. In-plane single-crystal-silicon microneedles for minimally invasive micro fluidic systems. Sens Actuators A. 2004;114:276–84.

Park JH, Davis S, Yoon YK, Allen MG, Prausnitz MR. Micromachined biodegradable microstructures. In: 16th IEEE international conference on microelectro mechanical systems. Kyoto, Japan. 2003. p. 371–74.

Park JH, Allen MG, Prausnitz MR. Biodegradable polymer microneedles: fabrication, mechanics and transdermal drug delivery. J Control Release. 2005;104(1):51–66.

Prausnitz MR. Microneedles for transdermal drug delivery. Adv Drug Deliv Rev. 2004;56:581–7.

Schreier H, Bouwstra J. Liposomes and niosomes as topical drug carriers-dermal and transdermal drug-delivery. J Control Release. 1994;30:1–15.

Schuetz YB, Naik A, et al. Emerging strategies for the transdermal delivery of peptide and protein drugs. Expert Opin Drug Deliv. 2005;2:533–48.

Shibata T, et al. Fabrication and mechanical characterization of microneedle array for cell surgery. In: Actuators and microsystems conference. 2007. p. 719–22.

Stoeber B, Liepmann D. Fluid injection through out-of-plane microneedles. Micro technologies in medicine and biology. In: 1st annual international conference. Berkeley, CA. 2000.

Stoeber B, Liepmann D. Design, fabrication and testing of a MEMS syringe. Berkeley sensor and actuator center, University of California at Berkeley, CA. 2002.

Sun C, Huang K. Numerical characterization of the flow rectification of dynamic microdiffusers. J Micromech Microeng. 2006;16:1331–9.

Timoshenko S, Krienger Woinowsky S. Theory of plates and shells. 2nd ed. New York: McGraw-Hill; 1995.

Wang X, et al. A novel fabrication approach for microneedles using silicon micromachining technology. In: 1st IEEE international conference on NEMS. 2006. p. 545–49.

Wang C, Leu T, Sun J. Unsteady analysis of microvalves with no moving parts. J Mech. 2007;23:9–14.

Wilke N, et al. Silicon microneedle electrode array with temperature monitoring for electroporation. Sens Actuators A. 2005a; 1090(123–124):319–25.

Wilke N, et al. Process optimization and characterization of silicon microneedles fabricated by wet etch technology. Micro Electron J. 2005b;36:650–6.

Yakhot A, Arad M, Ben-Dor G. Numerical investigation of a laminar pulsating flow in a rectangular duct. Int J Numer Methods Fluids. 1999;29:935–50.

Yao Q, Xu D, Pan L, Teo A, Ho W, Lee V, et al. CFD simulations of flows in valveless micropumps. Eng Appl Comput Fluid Mech. 2007;1:181–8.

Zahn JD, et al. Micro fabricated polysilicon microneedles for minimally invasive biomedical devices. Biomed Microdevices. 2000;2:295–303.

Zahn JD, et al. Continuous on-chip micropumping for microneedle enhanced drug delivery. Biomed Microdevices. 2004;6(3): 183–90.